Solvation Dynamics of the Electron Produced by Two-Photon Ionization of Liquid Polyols. 1. Ethylene Glycol

B. Soroushian,[†] I. Lampre,[†] J. Bonin,[†] P. Pernot,[†] S. Pommeret,[‡] and M. Mostafavi*[,†]

Laboratoire de Chimie Physique/ELYSE, UMR 8000 CNRS/Université Paris-Sud, Centre d'Orsay, Bât. 349, 91405 Orsay Cedex, France, and CEA/Saclay, DSM/DRECAM/SCM URA 331 CNRS, 91191 Gif-sur-Yvette Cedex, France

Received: July 20, 2005; In Final Form: October 28, 2005

Solvated electrons have been produced in ethylene glycol by two-photon ionization of the solvent with 263 nm femtosecond laser pulses. The two-photon absorption coefficient of ethylene glycol at 263 nm is determined to be $\beta = (2.1 \pm 0.2) \times 10^{-11}$ m W^{-1}. The dynamics of electron solvation in ethylene glycol has been studied by pump−probe transient absorption spectroscopy. So, time-resolved absorption spectra ranging from 430 to 710 nm have been measured. A blue shift of the spectra is observed for the first tens of picoseconds. Using the Bayesian data analysis method, the observed solvation dynamics are reconstructed with different models: stepwise mechanisms, continuous relaxation models, or combinations of stepwise and continuous relaxation. Comparison between models is in favor of continuous relaxation, which is mainly governed by solvent molecular motions.

1. Introduction

Since 1962 when it was first observed by transient absorption measurements in pulse radiolysis of water,[1−4] the solvated electron has been the subject of many studies. The solvated electron is characterized by an intense optical absorption band in the visible or near-infrared spectral domain depending on the solvent.[5] In water, the absorption band maximum is located at 715 nm while in less polar liquids it is situated in the near-infrared; for example, it is observed at 2200 nm in tetrahydrofuran (THF). For the series of alcohols, the absorption band maximum lies between 535 nm in glycerol and 820 nm in 2-propanol and it is around 575 nm in ethylene glycol (EG, 1,2-ethanediol). For the past decades, with the development of ultrashort laser pulses, much work has been devoted to the understanding of the electron localization and solvation in liquids. Studies on the formation of the solvated electron started in water.[6,7] Pump−probe laser experiments in neat water at very short times gave evidence that several precursors of the hydrated electron, absorbing mostly in the infrared domain, exist and that the hydration process is complete within a few hundreds of femtoseconds.[7] Subsequent geminate recombinations between hydrated electrons and hydronium cations or hydroxyl radicals occur on the picosecond time scale.[8−12] In alcohols, the formation of the solvated electron is slower than the formation in water allowing a better insight into the solvation processes and the precursor states.[13−15] For instance, it was reported that in methanol the solvation dynamics occurs in several steps followed by a slow process attributed to the cooling of the solvated electron as it relaxes in its ground state.[16]

Within this context, we will focus on the solvation dynamics of the electron in liquid polyols. The choice of the polyols comes from their relatively high viscosity (to slow any diffusion controlled process) and the presence of several hydroxyl groups, allowing investigation of the influence of the number and the distance between hydroxyl groups on the electron solvation process. First, we report the study in ethylene glycol (EG, 1,2-ethanediol), a solvent of great interest because it may be considered as a water analogue or alternatively regarded as two linked methanol molecules. Indeed, it is the simplest alcohol molecule with internal degrees of freedom, and it bears two hydroxyl groups which can form three-dimensional networks of hydrogen bonded molecules. Recently, the recombination dynamics of electrons produced in EG with UV femtosecond laser pulses, either by photodetachment of I^- ions or by two-photon ionization of the pure solvent, was studied from kinetics signals recorded at two different wavelengths.[17] In a previous preliminary paper on the formation of the solvated electron in pure EG by photoionization of the solvent with 263 nm femtosecond laser pulses, we presented time-resolved absorption spectra ranging from 450 to 725 nm and around 900 nm and analyzed the geminate recombination dynamics.[18] The electron ejection distances thus obtained were comparable to those reported for similar excitation energies in pure water. That study showed that the excess electron in EG presents a wide absorption band in the visible and near-IR domains at short delay times after the pump pulse and that the red part of the absorption band drops rapidly in the first few picoseconds while the blue part increases slightly.

In this paper, that study is resumed and deepened. As a first step, the two-photon absorption process leading to the solvent ionization is confirmed experimentally and the two-photon absorption coefficient of EG is determined as well as the photon absorption profile inside the sample. Then, the transient absorption spectra recorded in the visible domain for the first 50 ps are described. Moreover, the spectral evolution is fully analyzed using different models, stepwise and continuous relaxation mechanisms, to elucidate the initially formed species and the relaxation processes. Bayesian data analysis is performed to

* Corresponding author. E-mail: mehran.mostafavi@lcp.u-psud.fr.
[†] CNRS/Université Paris-Sud.
[‡] CEA/Saclay.

10.1021/jp0540149 CCC: $33.50
Published on Web 01/05/2006

obtain parametric identification and model comparison. This probabilistic method used, for instance, in environmental modeling[19] and biokinetics[20−22] is not commonly applied in data analysis of transient optical signals but has already been used with success.[23−25] In the present work, it has allowed us to analyze simultaneously and entirely all the kinetic traces, including the "coherent artifact" around time zero. On the basis of both the rigorous data analysis method and the comparison between the time-resolved spectra and the absorption spectra of the equilibrated solvated electron at different temperatures, the various models are compared and discussed in order to give an insight into the solvation dynamics of the electron in EG.

2. Experimental and Data Analysis Methods

2.1. Experimental Method. *2.1.1. Material.* Ethylene glycol from Aldrich (spectrophotometric grade) was used without further purification. The experiments were performed at room temperature.

2.1.2. Experimental Setup. Experiments were performed using a kilohertz femtosecond Ti:sapphire laser system (Spectra Physics) delivering laser pulses at 790 nm with a duration of 110 fs and an energy of 1 mJ. The pump beam at 263 nm (third harmonic) was produced by frequency doubling and sum-frequency mixing in two BBO (β-barium borate) crystals of 90% of the fundamental beam. Then, the pump beam was focused on a 300 μm thick ethylene glycol jet in order to produce solvated electrons by photoionization of the solvent. The pump beam diameter was usually set to 500 μm while the pump pulse duration and energy were about 210 fs full width at half-maximum (fwhm) and 20 μJ, respectively. As a probe beam, we used a white light continuum generated by 10% of the fundamental pulses at 790 nm in a 3 mm sapphire plate. A broad-band beam splitter divided the white light continuum into a probe and a reference beam. The probe beam was focused onto the EG jet using a 50 mm focal length achromat in order to minimize the chromatic focal shift and ensure a similar spatial repartition of all the wavelengths over the spot size. The estimated probe beam diameter was around 50 μm. After scanning the sample, the probe beam was dispersed on a polychromator and detected on a charge-coupled device (CCD) camera (1340 × 400 pixels, Princeton Instruments) with a resolution of 0.2 nm per pixel, simultaneously with the reference beam to take into account any laser fluctuations. A filter was placed just after the white light continuum generation to cut the residual Ti:sapphire fundamental beam and to avoid any nonlinear phenomena in the EG jet. As a chopper was also present on the pump path, the light absorption with and without the pump excitation was alternately monitored to ensure that the change in their ratio was due to the pump effects only. The addition of that chopper allowed us to improve the signal-to-noise ratio. Time-resolved absorption spectra ranging from 430 to 710 nm were recorded.

2.1.3. Nonlinear Measurements. For the nonlinear transmission experiments, the pump power density was increased on one hand by changing the pump beam diameter on the sample and on the other hand by varying the pump beam energy using a half-wave plate on the 790 nm beam. The incident and transmitted pump energy were measured just after the focusing lens and after the EG jet, respectively. The use of a jet allowed us to avoid any damage of cell windows and to eliminate any transient signals arising from cell windows at high power densities. Moreover, the flow of the EG jet was fast enough to ensure a complete renewal of the sample between two pulses (1 ms).

2.1.4. Group Velocity Dispersion. The group velocity dispersion was accurately determined by measuring the two-photon absorption in a thin silica plate with the 395 nm and the white light continuum pulses. The dispersion curve is defined by the position of the two-photon absorption maximum as a function of wavelength. It has been adjusted by a third-order polynomial of the wavelength λ:

$$t_0(\lambda) = p_0 + p_1\lambda + p_2\lambda^2 + p_3\lambda^3 \quad (1)$$

In our experiments using an EG jet, a coherent artifact structure, due to nonlinear phenomena induced by the temporal overlap of the pump and probe pulses in the EG jet, as already reported in previous experiments,[12,14,26,27] was observed at wavelengths below 600 nm. We checked that the wavelength dependence of the artifact maximum follows the same $t_0(\lambda)$ law (eq 1). This curve is therefore used afterward to synchronize the zero time for all wavelengths.

2.2. Data Analysis. *2.2.1. Data Conditioning.* Global analysis of the 2D spectrokinetics data matrix **D** is performed to enhance the identifiability of the kinetic and spectral parameters involved in the general expression for the transient absorbance

$$D_{ij} \cong \sum_{k=1}^{n} c_k(t_i)\, \epsilon_k(t_i, \lambda_j) \quad (2)$$

in the case of n absorbing species with concentration $c_k(t_i)$ as a function of time and molar extinction coefficient $\epsilon_k(t_i, \lambda_j)$ depending on time and wavelength.

Data over a 50 ps time span ($N_t = 180$ points per wavelength) and between $\lambda = 440$ nm and $\lambda = 710$ nm with a 5 nm step ($N_\lambda = 55$) have been considered. This represents a total of $N_D = 9900$ data points. Data are corrected for zero baseline. All other systematic effects are included explicitly in the model.

2.2.2. Bayesian Data Analysis. Analysis of spectrokinetics data has to face frequent issues in parametric identifiability. It is of utmost importance to go beyond conventional parameter optimization (i.e., using least-squares method) to get relevant information about the probability distribution of parameters involved in the models. Bayesian data analysis provides a consistent framework to deal with parameter optimization, parameter identification, and model selection. As this method is not frequently used in spectroscopy analysis, salient points are given here, and full accounts can be found in specialized literature.[28−30]

All information that can be inferred about the parameter set θ of model M are contained in the *posterior* probability density function (PDF), $p(\theta|\mathbf{D}, M)$, conditional to the data set (signals) **D** and model M. Optimization of $p(\theta|\mathbf{D}, M)$ with regard to θ provides the optimal set(s) of parameters called maximum a posteriori (MAP):

$$\hat{\theta} = \arg\max_\theta p(\theta|\mathbf{D}, M) \quad (3)$$

The average value and variance for a given parameter θ_i are obtained by

$$\langle\theta_i\rangle = \int \mathrm{d}\theta\, \theta_i\, p(\theta|\mathbf{D}, M) \quad (4)$$

and

$$\mathrm{Var}[\theta_i] = \int \mathrm{d}\theta\, (\theta_i - \langle\theta_i\rangle)^2\, p(\theta|\mathbf{D}, M) \quad (5)$$

Similarly, statistical estimates for any function f of θ are obtained from the posterior PDF as

$$\langle f \rangle = \int \mathrm{d}\theta\, f(\theta)\, p(\theta|\mathbf{D}, M) \tag{6}$$

Marginal densities are obtained by partial integration:

$$p(\theta_i|\mathbf{D}, M) = \int \mathrm{d}\theta_{-i}\, p(\theta|\mathbf{D}, M) \tag{7}$$

where the volume element excludes the parameter(s) of interest. Two-dimensional marginal densities

$$p(\theta_i, \theta_j|\mathbf{D}, M) = \int \mathrm{d}\theta_{-i,-j}\, p(\theta|\mathbf{D}, M) \tag{8}$$

are of key interest in the diagnostic of identification problem.

Multidimensional integrations necessary to Bayesian inference are actually performed by a Markov chain Monte Carlo (MCMC) method.[31] MCMC is used to get a representative sample of the posterior PDF which can then be used for any statistical operation. A Metropolis−Hasting algorithm was implemented with step sizes adjusted to get an acceptance ratio between 0.2 and 0.4. [31]

The posterior PDF depends on the *prior* PDF, $p(\theta|M)$, for the parameters and on the *likelihood* function $p(\mathbf{D}|\theta, M)$ through Bayes' rule:

$$p(\theta|\mathbf{D}, M) = p(\mathbf{D}|\theta, M)\, p(\theta|M)/p(\mathbf{D}|M) \tag{9}$$

The predictive probability $p(\mathbf{D}|M)$ can be used in model selection to quantify the performance of models. In cases where a single model is considered, it is a normalization constant, and its estimation is not required. The prior PDF should incorporate all information available on the parameters, independently of the data to be analyzed. The likelihood function quantifies the agreement of the model to the data for a given value of the parameters. It depends on the measurement errors. Assuming a uniform and unknown measurement error, we use here the function[30]

$$p(\mathbf{D}|\theta, M) = (R^2)^{-N_\mathrm{D}/2} \tag{10}$$

where R^2 is the sum of squares of residuals between model and data.

In the absence of a priori information, noninformative density functions for the prior PDFs are taken; that is, uniform PDFs for location parameters (for example, peak position) and log-uniform PDFs for scale parameters (such as lifetimes). This is the case for most parameters in the presented models; otherwise, prior PDFs are specified.

The interest of this approach is manifold:

- diagnostic detection of identifiability problems through visual inspection of density plots of 2D marginal PDFs;
- direct and accurate estimation of the uncertainties on the parameter values and easy uncertainty propagation to any function of the parameters;
- elimination of nuisance parameters through marginalization;
- consistent use of a priori information through the prior PDF.

2.2.3. Model Selection. Estimation of the predictive probability $p(\mathbf{D}|M)$ is generally tedious. Convenient approximations have been derived such as the Bayes information criterion (I_B) which is an index of model performance.[32] It weights the quality of the fit by the number of optimized parameters, and it is defined by

$$I_\mathrm{B}(M) = \ln p(\mathbf{D}|\hat{\theta}, M) - 0.5 N_\theta \ln N_\mathrm{D} = -0.5 N_\mathrm{D} \ln R^2|_{\hat{\theta}} - 0.5 N_\theta \ln N_\mathrm{D} \tag{11}$$

where $p(\mathbf{D}|\hat{\theta}, M)$ is the value of the likelihood at the MAP and N_θ is the number of optimized parameters. Better models are thus characterized by larger values of I_B.

The root-mean-square (rms) is often used as a criterion for fit quality:

$$\mathrm{rms} = \sqrt{\frac{1}{N_\mathrm{D}} R^2} \tag{12}$$

However, it cannot be reliable for comparison of models with different numbers of adjustable parameters while the maximization of I_B is a competition between minimization of rms and minimization of the number of parameters.

2.2.4. Semiparametric Models. The parameter space can be split into linear parameters θ_L and nonlinear parameters θ_NL. For a given value of θ_NL, it is possible to get optimized $\hat{\theta}_\mathrm{L}$ by a fast linear least-squares method, which defines a functional relation $\hat{\theta}_\mathrm{L} = f(\theta_\mathrm{NL})$. This is a rigorous optimization approach only if measurement noise can be considered as normal and additive and if the prior PDF for the linear parameters is uniform (which is the case for the present study). However, this approach does not enable a proper estimation of the uncertainties on the nonlinear parameters.

This parameter separation can be applied with profit in our case when contributions to the absorbance signal A_{ij} at a given time t_i and energy E_j (i.e., wavelength λ_j) can be factorized as linear forms:

$$A_{ij} = \sum_k C_k(t_i, E_j; \theta_\mathrm{NL})\, \epsilon_k(E_j) \tag{13}$$

The linear parameters are the energy dependent extinction coefficient $\epsilon_k(E_j)$. These $(n \times N_\lambda)$ parameters are determined by minimizing a partial sum over squared residuals R_j^2, where the sum runs only over the time variable:

$$R_j^{\,2} = \sum_{i=1}^{N_t} (D_{ij} - \mathrm{A}_{ij})^2 \tag{14}$$

with constraints $\epsilon_k(E_j) > 0$. As this approach enables us to avoid the definition of an explicit parametric shape (as Gaussian, log-normal, etc.) for absorption spectra, and in reference to nonparametric modeling, we call it semiparametric modeling in the following.

3. Experimental Results

As demonstrated for multiphoton ionization of water, the number of absorbed photons, that is, the available excess energy, is an important parameter for the subsequent electron dynamics.[10] Consequently, before studying the solvation dynamics of the electron in ethylene glycol, the ionization process must be analyzed. Since the ionization threshold of liquid EG is known to be 8.3 ± 0.1 eV [33] and the energy of 263 nm photons is 4.7 eV, the ionization of liquid EG should proceed via a two-photon absorption mechanism.

3.1. Two-Photon Absorption at 263 nm. The transmittance of the 300 μm EG jet versus the peak power of the 263 nm input pulse is shown in Figure 1. The evolution is characteristic of a single-beam, two-photon absorption (SB−TPA).[6,9,34] In that case, the differential equation describing the optical loss along the optical path length z is given by[35,36]

$$\frac{1}{I(z, r, t)} = \frac{\partial I(z, r, t)}{\partial z} = -\beta I(z, r, t) \tag{15}$$

where $I(z, r, t)$ (z, r, and t are the cylindar coordinates) is the

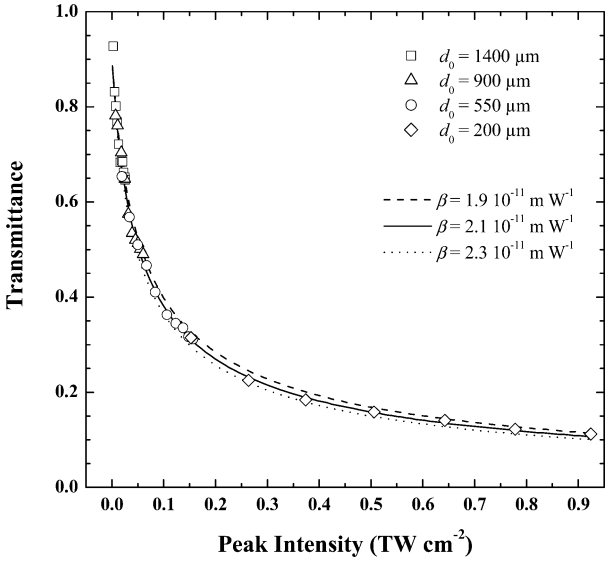

Figure 1. Two-photon absorption in neat liquid ethylene glycol at 263 nm. Transmittance of the 300 μm EG jet versus the peak intensity of the 220 fs input pulse is shown. ((symbols) experimental data for four different beam diameters; (lines) calculated curves using eq 18 for different values of β and $R = 0.05$).

irradiance and β is the SB−TPA coefficient characterizing the material and expressed in units of m W^{-1}. If we assume that the incident pulse shape $I_0(r, t)$ is given by Gaussian functions in time (t) and in transverse coordinate (r),

$$I_0(r, t) = I_0 \exp\left(-4 \ln 2 \frac{r^2}{{d_0}^2}\right) \exp\left(-4 \ln 2 \frac{t^2}{{\sigma_0}^2}\right) \quad (16)$$

where σ_0 stands for the pulse duration (fwhm), d_0 for the beam diameter, and I_0 for the peak irradiance. Then the total energy (E_0) contained in the incident pulse is obtained by integrating $I_0(r, t)$ over the time and transverse coordinates and is related to the peak irradiance (I_0) by

$$I_0 = \left(\frac{4 \ln 2}{\pi}\right)^{3/2} \frac{E_0}{\sigma_0 {d_0}^2} \quad (17)$$

The measured transmittance (T) of the EG jet corresponds to the ratio of the transmitted pulse energy (E) to the incident pulse energy (E_0). The integration of eq 15 gives

$$T = \frac{E}{E_0} = \frac{(1 - R)^2}{E_0} \int_0^\infty \mathrm{d}r\, 2\pi r \int_{-\infty}^{\infty} \mathrm{d}t \frac{I_0(r, t)}{1 + \beta L (1 - R) I_0(r, t)} \quad (18)$$

where R denotes the Fresnel reflection losses at the air−EG jet interfaces and L is the jet thickness. Using eq 18 to fit our experimental values of the transmittance (T) as a function of the peak irradiance (I_0), we determine the values of β and R: $\beta = (2.1 \pm 0.2) \times 10^{-11}$ m W^{-1} and $R = 0.05$ (Figure 1).[37] The present value of β for EG at 263 nm is close to the value ($\beta = (1.8 \pm 0.4) \times 10^{-11}$ m W^{-1}) obtained for water at 266 nm with 100 fs pulses.[34] However, this β value is 1 order of magnitude higher than the literature values that were obtained with 266 nm picosecond laser pulses for water[6] and measured for several liquids at 264 nm with 200 fs pulses but on a much lower intensity domain ($I_0 < 30$ GW/cm^2).[38]

3.2. Two-Photon Absorption Profile. The amount of energy absorbed per unit of time and volume (irradiance deposit distribution, IDD(z, r, t)) is derived from eq 15, neglecting the deformation of the propagating pulse:

$$\mathrm{IDD}(z, r, t) = -\frac{\partial I}{\partial z}(z, r, t) = (1 - R)^2 \beta_2 \frac{{I_0}^2(r, t)}{[1 + \beta z (1 - R) I_0(r, t)]^2} \quad (19)$$

If one divides by the photon energy ($h\nu$) and integrates over time, the profile of absorbed photons per pulse $C_p(z, r)$ is obtained:

$$C_p(z, r) = \frac{1}{h\nu N_A} \int_{-\infty}^{+\infty} \mathrm{IDD}(z, r, t)\, \mathrm{d}t \quad (20)$$

where N_A is the Avogadro number. According to eqs 16, 19, and 20, $C_p(z, 0)$ is the maximum longitudinal concentration profile (MLCP) of absorbed photons along the EG jet while the mean radial concentration profile (MRCP) of absorbed photons is defined by the equation

$$\mathrm{MRCP}(r) = \frac{1}{L} \int_0^L C_p(z, r)\, \mathrm{d}z \quad (21)$$

Figure 2 shows the concentration profiles calculated for two peak power densities ($I_0 = 0.05$ and 0.15 TW/cm^2) using the β and R values determined in the previous section and a pump beam diameter of $d_0 = 550$ μm. We note that the longitudinal profile $C_p(z, 0)$ depends greatly on the peak power intensity in contrast to the radial profile MRCP(r). When the peak power density is increased, the MRCP broadens and becomes almost identical to the pump pulse profile (parts A1 and B1 of Figure 2). At high irradiance (Figure 2, B2), the initial value of $C_p(z, 0)$ is high (0.017 mol L^{-1}). Then $C_p(z, 0)$ drops greatly in the first tens of micrometers (at $z = 95$ μm, $C_p(z, 0) = 1.7 \times 10^{-3}$ mol L^{-1}). In contrast, at low irradiance (Figure 2, A2), the initial value of $C_p(z, 0)$ is smaller (1.7×10^{-3} mol L^{-1}) and $C_p(z, 0)$ decreases more slowly along the whole jet thickness to reach 0.17×10^{-3} mol L^{-1} at 300 μm, the jet thickness. Thus, high power densities generate high but strongly nonuniform electron concentrations along the jet compared to the smaller concentrations produced at low power densities.

In a previous work on the hydrated electron,[34] we showed that the change in the pump power density affects not only the electron concentration but also the kinetics. Indeed, the kinetics obtained at high power densities cannot be described within the theoretical framework developed for the geminate recombination in dilute solution using the independent pair approximation. In the following study on the electron in EG, we used low peak power densities ($\leq$0.1 TW/cm^2), so there is no influence of electron concentration on the observed dynamics at short times ($t < 500$ ps). In ref 18, we showed that the normalized signals recorded with different low power densities were superimposable indicating that the same phenomena occur whatever the low power density and that the solvation dynamics are independent of the electron concentration in our experimental conditions.

3.3. Formation of Solvated Electrons in EG. Figure 3a shows the transient absorption signals recorded over 50 ps at three different wavelengths upon photoionization of EG. For clarity reasons, the signals are not corrected for the group velocity dispersion. During the pulse duration, the "coherent artifact" is observed for wavelengths below 600 nm. After the artifact, we observe that the signals at 560 and 440 nm rise fast for about 5 ps, then remain quasi-constant for the next 40 ps;

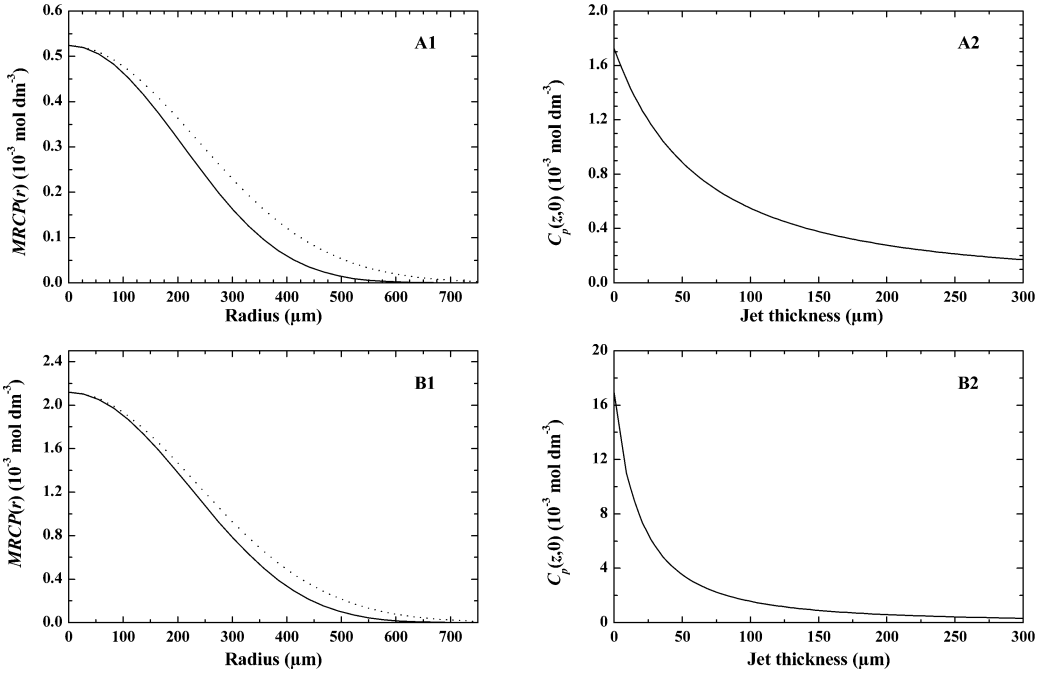

Figure 2. Absorbed photon concentration profiles for two-photon absorption at 263 nm inside the 300 μm EG jet calculated for two peak intensities ((A) 0.05 TW/cm^2; (B) 0.15 TW/cm^2) according to eqs 20 and 21 with $\beta = 2.1 \times 10^{-11}$ m W^{-1}, $R = 0.05$, $d_0 = 550$ μm. The dotted line represents input spectral profile $I_0(r, t = 0)$.

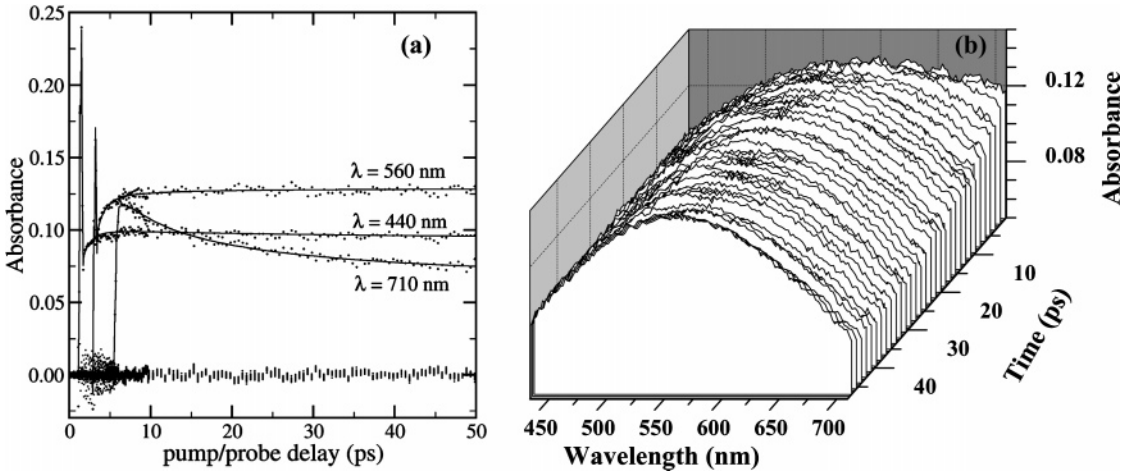

Figure 3. (a) Transient absorption signals at three different wavelengths and (b) time evolution of the absorption spectrum obtained upon photoionization of ethylene glycol at 263 nm. For clarity reasons, the kinetics signals are not corrected for the group velocity dispersion contrary to the spectra. The solid lines drawn through the points correspond to the best fit obtained with a continuous relaxation model (CRELH).

there are a tiny increase in the signal at 560 nm and a slight decrease at 440 nm. In contrast, the absorbance measured at 710 nm decreases continuously.

Figure 3b presents the time evolution over 50 ps of the absorption spectrum obtained in EG after photoionization of the solvent at 263 nm. It is to be noted that the spectra are corrected for the group velocity dispersion and that, for clarity of presentation, the first plotted spectrum corresponds to a time delay of 500 fs; consequently the coherent artifact around zero time delays is not present on the figure.

We remark that the main change occurs in the red part of the spectrum. At early time, a very broad absorption band with a maximum around 675 nm is observed. For the first 5 ps, the spectrum shifts to shorter wavelengths and its maximum absorbance increases slightly as the blue part of the absorption band (below 620 nm) rises and the red part decreases. So, the absorption band maximum is located around 590 nm at 5 ps. Then, the absorbance on the red side of the spectrum follows its decrease while the absorbance on the blue side (below 570 nm) remains constant. Consequently, the absorption spectrum becomes less broad and its maximum continues to shift toward the blue spectral domain to reach around 50 ps at 570 nm (2.17 eV), nearly the absorption band maximum of the solvated electron in ethylene glycol.

4. Data Analysis and Discussion

4.1. Models for Solvation Dynamics. The solvation of an excess electron in polar liquids is a subject under debate.[7,12,16,39−42] It is still unclear if the relaxation proceeds stepwise, by continuous relaxation, or by a combination of both mechanisms. We found it worthwhile to evaluate those hypotheses with a meticulous data analysis. For all the models, we first need to fit the coherent artifact around the time zero.

4.1.1. Artifacts around Time Zero. The structure of the signals observed around time zero mostly in the blue part of the spectral

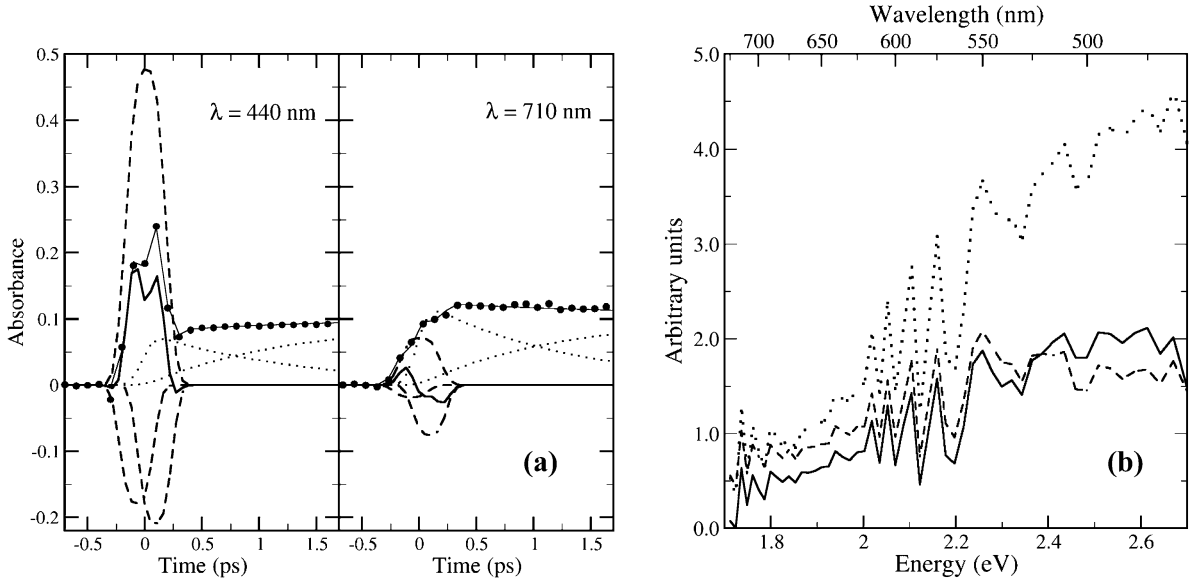

Figure 4. (a) Examples of the time-symmetric combinations of three generalized Gaussian functions (- - -) used to describe the "coherent artifact" (—) and fit our data (closed circles). The thin line drawn through the points corresponds to the best fit obtained with a stepwise mechanism (STEP3P), with the dotted lines giving the contributions of the first two species to the signal. (b) Spectral dependence of the amplitude $a_i(E)$ of three generalized Gaussian functions used to fit the "coherent artifact"; (—) $a_1(E)$, (•••) $a_2(E)$, (- - -) $a_3(E)$.

domain is due to the superimposition of several effects onto the transient absorption signal. In the present experimental conditions, cross-phase modulation (XPM) is considered to be the main source of the coherent artifact, with probably a contribution of two-photon (one pump + one probe) absorption by EG since the absorption threshold of EG is 6.5 eV.[33] The shape of the artifact signal in the pump−probe experiments has already been much discussed in the literature, but presently there is no consensus on the best way to model that effect.[27,43−45] For example, Lorenc et al. recently proposed an approximate formula for XPM.[43] This model, characterized by negative and positive absorbance contributions of similar amplitudes, could not be adjusted to our data, which display a very marked positive peak (Figure 3a). Instead, to describe the part of the signals due to the artifact, we used a time-symmetric combination of three generalized Gaussian functions:

$$A_0(t, E) = -a_1(E)\,\mathcal{G}(t; t_0(E) - \Delta, \gamma_1, \alpha) + a_2(E)\,\mathcal{G}(t; t_0(E), \gamma_2, \alpha) - a_3(E)\,\mathcal{G}(t; t_0(E) + \Delta, \gamma_1, \alpha) \quad (22)$$

with

$$\mathcal{G}(t; t_0, \gamma, \alpha) = \exp\left(-\left|\frac{t - t_0}{\gamma}\right|^{\alpha}\right) \quad (23)$$

and $\alpha \geq 2$. Note that $t_0(E)$ corresponds to the group velocity dispersion curve (eq 1) in energy space. The generalized Gaussian parameters are found to be $\Delta = 86 \pm 2$ fs, $\gamma_1 = 0.165 \pm 0.001$, $\gamma_2 = 0.202 \pm 0.001$, and $\alpha = 3.5 \pm 0.1$. Figure 4a presents the determined contributions of the coherent artifact to the kinetic traces at two different wavelengths. Spectral shapes $a_i(E)$ of XPM contributions were obtained point by point using the semiparametric procedure described above. As can be seen in Figure 4b, the spectral behavior of the three components is strongly oscillatory, and we did not attempt to model it.

4.1.2. Stepwise Models. First, we considered sequential stepwise relaxation cascades, commonly used to depict the electron solvation process.[9,14,16,39,46] Every one of the n considered species or states of the electron is supposed to have a fixed, individual spectrum. The absorbance is then written as

$$A(t, E) = A_0(t, E) + \mathcal{G}(t; t_0(E), \sigma/\sqrt{4 \ln 2}, 2) \otimes \sum_{k=1}^{n} c_k(t)\,\epsilon_k(E) \quad (24)$$

where the Gaussian function $\mathcal{G}(t; t_0(E), \sigma/\sqrt{4\ln 2}, 2)$ models the instrumental response function (cross correlation of the pump and probe pulses) and the ⊗ symbol stands for the convolution operator. The concentration curves $c_k(t)$ are obtained analytically by the standard Laplace transform method. Spectra have been determined point by point, $\epsilon_k(E_j)$, or modeled by a log-normal shape function S:

$$\epsilon_k(E) = \epsilon_k\, S(E; E_{\max,k}, \Omega_k, \gamma_k) \quad (25)$$

where the function S is parametrized by the peak position $E_{\max}$, the full width at half-maximum Ω, and the asymmetry factor γ (see Appendix). To take into account the asymmetry of the absorption spectrum, the use of a unique log-normal function[47] was preferred to the usual model where the low- and high-energy sides of the solvated electron spectrum are described by Gaussian and Lorentzian shape functions, respectively.[48,49] We used noninformative prior PDFs for all parameters.

4.1.3. Continuous Relaxation Models. Another proposed way to interpret the dynamics events occurring during electron solvation is to consider only one localized species whose spectrum undergoes a continuous evolution.[12,50,51] The time-dependent absorption spectrum is then described by a log-normal function with time-dependent coefficients:

$$A(t, E) = A_0(t, E) + \mathcal{G}(t; t_0(E), \sigma/\sqrt{4 \ln 2}, 2) \otimes [c_0\,\epsilon(t) \times S(E; E_{\max}(t), \Omega(t), \gamma(t))] \quad (26)$$

To account for solvation sites and/or relaxation rates heterogeneity, the time-dependence of each parameter ($x = \epsilon$, $E_{\max}$, Ω, γ) is modeled either by a multiexponential function,

$$x(t) = x_\infty + \sum_i \Delta_{x,i}\,\mathcal{G}(t; 0, \tau_{x,i}, 1) \quad (27)$$

or by a specific stretched exponential function as in models used

TABLE 1: Comparison between the Different Models Used To Fit the Experimental Data on the Solvation of the Electron in Ethylene Glycol

model name	scheme	comments	N_θ[a]	rms[b]	I_B[c]
		Semiparametric Models			
STEP2	$e^-_{wb} \rightarrow e^-_s$	one-step process	56	3.57×10^{-3}	9989
STEP3	$e^-_{wb} \rightarrow e^-_{sb} \rightarrow e^-_s$	two-step process	112	2.54×10^{-3}	13092
STEP4	$e^-_{wb} \rightarrow e^-_b \rightarrow e^-_{sb} \rightarrow e^-_s$	three-step process	168	2.43×10^{-3}	13282
PAR3	$e^-_{wb,1} \rightarrow e^-_s$ $e^-_{wb,2} \rightarrow e^-_s$	two relaxing species	112	2.54×10^{-3}	13092
		Parametric Models			
STEP3P	$e^-_{wb} \rightarrow e^-_{sb} \rightarrow e^-_s$	two-step process	9	2.56×10^{-3}	13509
CREX1	$e^-_{wb} - - \rightarrow e^-_s$	homogeneous relaxation	8	2.83×10^{-3}	12516
CREX2	$e^-_{wb} - - \rightarrow e^-_s$	biexponential relaxation	10	2.47×10^{-3}	13846
CREX3	$e^-_{wb} - - \rightarrow e^-_s$	triexponential relaxation	11	2.47×10^{-3}	13871
CRELH	$e^-_{wb} - - \rightarrow e^-_s$	heterogeneous relaxation	10	2.50×10^{-3}	13730
HYB	$e^-_{wb,1}{}^* - - \rightarrow$ ($\downarrow$ $\downarrow$ $\downarrow$) $e^-_{sb,2}{}^* - - \rightarrow e^-_s$	one step between two relaxing species	9	2.67×10^{-3}	13088
HYBM	$e^-_{wb,1} \cdots$ ($\downarrow$ $\downarrow$) $e^-_{sb,2}{}^* - - \rightarrow e^-_s$	one step and homogeneous relaxation	13	2.53×10^{-3}	13623

[a] Number of adjusted parameters excluding "coherent artifact". [b] Root mean square. [c] Bayes information criterion.

to describe the relaxation behavior of glass-forming liquids or time-resolved Stokes shift fluorescence data:[52]

$$x(t) = x_\infty + \Delta_x \mathcal{G}(t; 0, \tau_x, \beta_x); \quad 0 < \beta_x \leq 1 \qquad (28)$$

In that case, for each parameter x, two characteristic times can be defined in terms of the function Γ: the average relaxation time given by $\langle\tau_x\rangle = \tau_x\beta_x^{-1}\,\Gamma(\beta_x^{-1})$, and the average lifetime $\langle t_x\rangle = \tau_x\,\Gamma(2\beta_x^{-1})/\Gamma(\beta_x^{-1})$. The departure from homogeneity has to be ascertained by the data. So, we chose to favor high values of β parameters by taking β density functions as prior PDFs: $p(\beta|M) = \beta(2, 0.75)$. This function is strongly peaked near $\beta = 1$ but is nonvanishing for smaller values.

4.1.4. Hybrid Models: Stepwise + Continuous Relaxation. The necessity to include both stepwise mechanism and continuous relaxation to successfully interpret experiments has also been suggested. A "hybrid" solvation model has been developed by Pépin and co-workers.[27,40] This model is characterized by two unrelaxed trapped species, $e^-_{wb,1}$ and $e^-_{sb,2}$, whose spectra shift continuously to the blue; $e^-_{wb,1}$ transforms into $e^-_{sb,2}$ via a stepwise transition with a characteristic time τ_{12}, and $e^-_{sb,2}$ is modeled to relax continuously into the fully solvated electron. The absorbance is then written as

$$A(t, E) = A_0(t, E) + \mathcal{G}(t; t_0(E), \sigma/\sqrt{4\ln 2}, 2) \otimes c_0\{p_1 \exp(-t/\tau_{12})\,\epsilon_1 S(E; E_{\max,1}(t), \Omega_1, \gamma_1) + [p_2 + p_1(1 - \exp(-t/\tau_{12}))]\,\epsilon_2(t) \times S(E; E_{\max,2}(t), \Omega_2(t), \gamma_2(t))\} \qquad (29)$$

where p_1 (p_2) represents the proportion of electron directly trapped into the $e^-_{wb,1}$ ($e^-_{sb,2}$) electron−solvent configuration.

In the model used by Pépin et al., the absorption spectra of both species are assumed to remain constant in shape (determined by Ω and γ) and amplitude (ϵ) during the whole solvation process and just to translate along the energy axis with the same characteristic time τ_{cont}. However, this model can be extended using time-dependent absorption spectra with exponentially time-dependent parameters (ϵ, E_{max}, Ω, γ) in the framework of homogeneous relaxation model (monoexponential function, eq 27, or heterogeneity parameters equal to 1: $\beta_{E_{max}} = \beta_\Omega = \beta_\gamma = \beta_\epsilon = 1$, eq 28).

4.2. Data Analysis. According to our previous work,[18] the geminate recombination of the electron in EG is very slow and we have checked that it can be neglected in the time-window of the present study. Consequently, the final species in our models, the solvated electron, can be considered to be stable and to have an infinite lifetime. However, the spectral evolution is not fully achieved in the measurement time interval. So, the solvated electron spectrum, already known from pulse radiolysis measurements, was explicitly introduced in the models. Its parameters $E_{max,\infty} = 2.219 \pm 0.001$ eV, $\Omega_\infty = 1.208 \pm 0.002$ eV, and $\gamma_\infty = 1.461 \pm 0.008$ have been obtained by fitting the absorption spectrum measured at long time with a log-normal function. In that case, the Bayesian index I_B is worth 3704 against a value of 3572 if the fit is performed with a Gaussian−Lorentzian model. In the literature, there is a disagreement on the value of the extinction coefficient at the maximum of the solvated electron absorption band in EG. Sauer et al. gave the value of 14 000 M^{-1} cm^{-1}, [53] based on a radiation chemical yield for e^-_s of 1.2 molecules/100 eV. Jou and Freeman later confirmed that the product of ϵ by G in $(CH_2OH)_2$ was around $(1.7-1.8) \times 10^4$ M^{-1} cm^{-1}/100 eV. [54] However, the solvated electron yield of 1.2 molecules/100 eV reported by Sauer et al. (1965) is clearly too small in the light of comparison with the yield in other solvents such as methanol or ethanol. Therefore, considering a value of G close to 2, the extinction coefficient at maximum has been fixed to $\epsilon_\infty = 9000$ M^{-1} cm^{-1}. Nevertheless, that value does not affect the absorption band shapes and the kinetics data issued from the different models used in the present work.

4.2.1. Stepwise Modeling. To assess the simplest and most used mechanism, we applied sequential models. First, all spectra have been left unconstrained in the framework of the semiparametric method. In that case, due to the limited time window (<50 ps), the asymptotic solvated electron spectrum is not recovered and the lifetimes are biased accordingly. We stress that, to circumvent this problem, it is necessary to introduce explicitly the solvated electron spectrum, that is, $\epsilon_n(E_j) = \epsilon_\infty S(E_j; E_{max,\infty}, \Omega_\infty, \gamma_\infty)$.

Models with two (STEP2), three (STEP3), and four (STEP4) states or species have been tested (Table 1). It appears that at least three states are necessary and sufficient to properly fit the

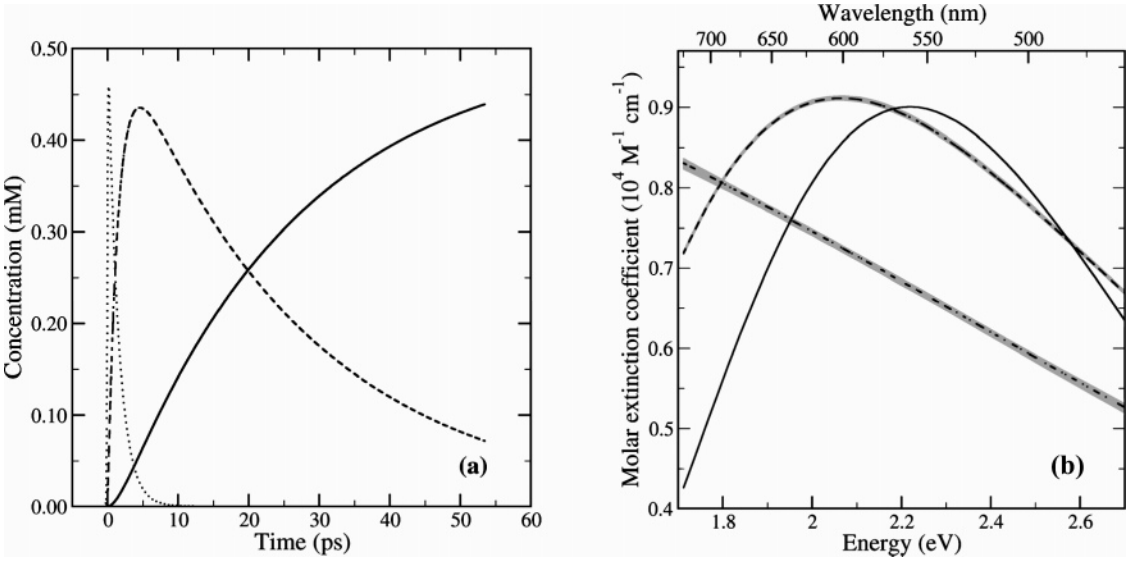

Figure 5. (a) Time evolution of the concentrations and (b) absorption spectra of the three species involved in the stepwise mechanism (STEP3P) used to fit the experimental data: (•••) e^-_{wb}, (- - -) e^-_b, and (—) e^-_s. The gray areas represent the fluctuation of the spectra, given data uncertainty.

TABLE 2: Parameters of STEP3P Model Resulting from the Probabilistic Analysis of the Experimental Data for the Solvation of the Electron in Ethylene Glycol

	e_{wb}	e_{sb}	e_s
ϵ (M^{-1} cm^{-1})	10310 ± 510	9120 ± 40	9000
E_{max} (eV)	0.4 ± 0.2	2.064 ± 0.001	2.219
Ω (eV)	4.7 ± 0.3	1.613 ± 0.002	1.208
γ	1	2.085 ± 0.006	1.461
τ (ps)	1.31 ± 0.01	25.0 ± 0.2	

data. A simple mechanism with only two species (STEP2) is excluded. Fit quality is slightly enhanced with a third intermediate state (STEP4), but then, the spectra display a regular evolution from state to state which strongly suggests a continuous relaxation process.

We have retained the three-state model (STEP3) as a reference for the stepwise procedure and treated it with a fully parametric model (STEP3P). The loss in rms due to the full parametrization of the spectra is negligible, considering the enormous reduction in the number of free parameters. In the studied energy domain, the log-normal shape for absorption spectra of electrons is thus a very good model. We found it to provide better fits than the commonly used Gaussian/Lorentzian shape. The optimal spectra and kinetics are displayed in Figure 5. Values of the parameters are reported in Table 2. Being located outside of the observation window, the position of the absorption maximum for the weakly bound electron e^-_{wb} is poorly identified. Similarly, its asymmetry factor was unidentified and has been fixed to 1.

According to this model (Figure 5a and Table 2), the intermediate species, e^-_{sb}, builds up from the initially generated electron with a time constant τ_1 of 1.3 ± 0.1 ps and slowly gives the solvated electron, e^-_s, with a time constant τ_2 equal to 25.0 ± 0.2 ps. These times are much longer than the times obtained in water for the formation and decay of the presolvated electron (110 and 240 fs, respectively),[55] which can be explained by the high viscosity of EG and its lower dielectric constant. However, they are closer to the times determined in other alcohols.[14,16] In particular, for the series of linear alcohols such as methanol, ethanol, and butanol, Shi et al.[14] found an increase in the formation time of the solvated electron with the chain length (7.1 ± 0.3 ps in methanol, 15 ± 1 ps in ethanol, and 33 ± 3 ps in butanol). The effect of the increased mass of the longer chain was attributed to a slowing down of the librational and translational motions of the alcohol molecules, which increases the time to achieve the optimal configurations. The value obtained for τ_2 is larger than that determined by Shi et al. in ethanol,[14] which is in agreement with an expected mass effect of the additional OH group.

The absorption spectra of the three species involved in the STEP3P model are shown in Figure 5b. The first species, e^-_{wb}, appearing after ionization of EG, presents a structureless absorption in the visible domain. The absorption maximum of e^-_{wb} is out of the investigated spectral range, in the infrared domain. The second species, e^-_{sb}, exhibits a quite broad absorption band in the visible domain with a maximum around 600 nm. This band is close to that of the solvated electron, e^-_s, in the high-energy side, indicating the quick formation of well-localized electrons despite the high solvent viscosity (~16 times that of water) and suggesting the presence of preexisting traps in the solvent. We note that, notwithstanding a large uncertainty on the peak position of the absorption band of e^-_{wb} (Table 2), uncertainty propagation reveals that the spectrum is fairly determined in the studied spectral window (Figure 5b).

It is to be noted that a parallel mechanism with three states (PAR3) provides a fit as good as the sequential model. However, the corresponding spectra display structures which are not expected from a solvated electron (Figure 6). Thus, we did not further consider that model.

4.2.2. Continuous Relaxation Modeling. First, we performed a fit considering a homogeneous relaxation with monoexponential time dependences, that is, with all heterogeneity parameters β_x set to 1 (eqs 26−28). This homogeneous relaxation model (CREX1, Table 1) is unable to correctly reproduce the data. However, this description becomes valid for delays larger than 5 ps. Then, models dealing with two (CREX2) and three (CREX3) exponential functions were tested (Table 1). We note that biexponential functions provide a very good fit of the data and that addition of a third exponential component does not improve much the fit quality (similar rms and I_B values). Values of the parameters determined with CREX2 model are reported in Table 3. As unconstrained adjustments had led to very close values (within the uncertainties) and as the short time was undetermined for γ, the characteristic times have been constrained to be the same for

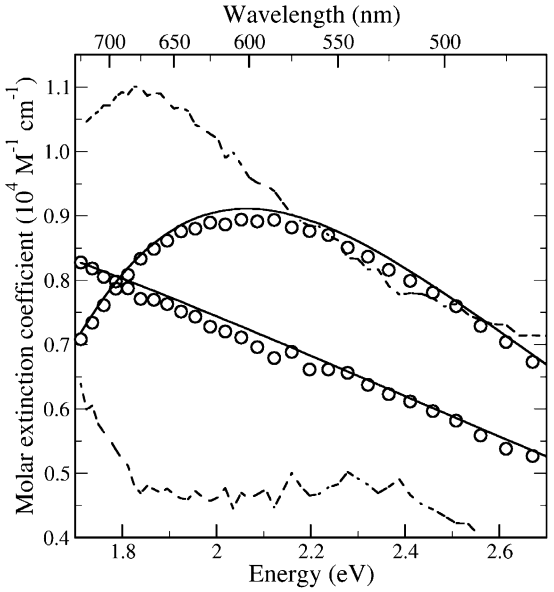

Figure 6. Absorption spectra obtained with a semiparametric ((○) STEP3) or a fully ((—) STEP3P) parametric method for the first two species involved in a two-stepwise mechanism and absorption spectra of the two initial species in the case of a parallel mechanism with three states ((- - -) PAR3).

E_{max}, Ω, and γ. Moreover, the kinetics of ϵ appeared to be monoexponential. The values obtained for the characteristic times ($\tau_\epsilon \cong 1$ ps, $\tau_{E_{max}1} = \tau_{\Omega 1} = \tau_{\gamma 1} \cong 1.7$ ps, and $\tau_{E_{max}2} = \tau_{\Omega 2} = \tau_{\gamma 2} \cong 25.5$ ps) are in the neighborhood of those determined with STEP3P ($\tau_1 \cong 1.3$ ps, $\tau_2 \cong 25.0$ ps). The average lifetimes are dominated by the long time component ($\langle\tau_x\rangle \geq 22.5$ ps). The fast increase in the peak intensity within about 1 ps may suggest a delay in the formation of the solvated electron, which is comparable to the τ_1 value in the STEP3P model.

As often used to depict nonexponential relaxations in disordered materials, we also considered stretched exponential type decays for the parameters (CRELH model). Heterogeneity parameters β_x have then been allowed to vary (eqs 26 and 28) leading to a good adjustment of data but not as good as CREX2 (Table 1). Two parameters (E_{max} and Ω) appear to have strongly heterogeneous dynamics ($\beta_x < 0.5$), whereas the peak intensity ϵ increases exponentially (Table 4) as for CREX2. The asymmetry factor γ has also a single exponential dynamics, mostly because its evolution cannot be accurately followed at short times. With the CRELH model, we find similar relaxation times for ϵ and E_{max} (~1 ps) on one hand and for Ω and γ (~6.4 ps) on the other hand, but as the heterogeneity parameters β_x differ, the average relaxation times $\langle\tau_x\rangle$ as well as the average lifetimes $\langle t_x\rangle$ for each parameter are different. We note that, for E_{max} and Ω, the two average times differ significantly from each other due to the small values of β_x and also from the other characteristic times determined with CREX2 or STEP3P models. Values for the average relaxation time $\langle\tau_x\rangle$ (5.5 and 14.3 ps) are shorter than the value of 25 ps while the values of the average lifetimes ($\langle t_x\rangle$) are close (46.4 and 47.2 ps) but higher than 25 ps.

Figure 7 describes the time-dependence of the different parameters (ϵ, E_{max}, Ω, γ) determined in the case of the continuous relaxation with CREX2 and CRELH models. We remark that, while the time evolution of ϵ is identical, the evolution drawn for γ differs greatly from one model to the other, showing that this parameter is not well defined in our experimental conditions because of the restricted spectral window. The time evolutions for the peak position E_{max} and the bandwidth Ω obtained with both models are nearly superimposed, the main difference occurring around time zero. That should come from the fact that the derivative of the stretched exponential function diverges as $t \rightarrow 0$; so there are always very fast contributions, faster than our experimental resolution (<500 fs). Those fast contributions are balanced by long time components, responsible for the relatively long lifetimes (around 45 ps). Consequently, the values of $\beta_x < 0.5$ obtained for E_{max} and Ω correspond to very broad distributions of exponential relaxation times making difficult the physical interpretation of the stretched exponential function. However, despite few discrepancies in the time evolution of the parameters, the time-resolved spectra obtained with both models are very similar (Figure 8).

4.2.3. Hybrid Models. The hybrid model of Pépin and coworkers (HYB, eq 29) applied to our data does not provide a fit as good as STEP3P with the same number of adjustable parameters (Table 1). Moreover, the values found for the parameters are not physically acceptable. Indeed, the best fit is obtained for a weakly bound electron $e^-_{wb,1}$ with a long lifetime ($\tau_{12} = 32.4$ ps) but without spectral shift ($\Delta_{E_{max,1}} = 0$) and a quite short characteristic time of the spectral blue shift ($\tau_{cont} = 1.3$ ps). To improve the fit quality, we modified the hybrid model (HYBM): $e^-_{wb,1}$ does not relax and undergoes only the stepwise transition into the relaxing $e^-_{sb,2}$ whose absorption spectrum varies in energy but also in amplitude and shape with different characteristic times. Optimization of the parameters for this model (HYBM, Table 5) revealed that the continuous relaxation of $e^-_{sb,2}$ to e^-_s can be fitted by a homogeneous or exponential model ($\beta_{E_{max}} = \beta_\Omega = \beta_\gamma = \beta_\epsilon = 1$). The characteristic relaxation rates for all properties, except ϵ(t), are very close ($\tau_{E_{max}} = \tau_\gamma \simeq \tau_\Omega \simeq 25$ ps) while the absorbance parameter presents a faster component ($\tau_\epsilon \simeq 2.1$ ps). The characteristics of the weakly bound electron $e^-_{wb,1}$ appear reasonable ($\tau_{12} = 2.40 \pm 0.03$ ps and Figure 9). The weakly bound electron is initially the preponderant species ($p_1 = 0.88$), only a small portion of electron being directly trapped into the $e^-_{sb,2}$ state ($p_2 = 0.12$). Existence of two initial trapped electrons might be related to the presence of both gauche and trans conformers in liquid-state EG. Numerous experimental and theoretical studies on the molecular structure of EG indicate strong preferences for the gauche conformation with involvement of the intramolecular H bond.[56−60] However, there are some discrepancies in the quantitative estimate of the fraction of molecules in the trans conformers in pure EG: Patchler and Wessels reported a proportion of gauche conformers of ~86%[56] while Schwartz determined the percentage of trans conformers to be ~35%.[57]

4.3. Discussion. If we compare the results of the Bayesian analysis of our spectrokinetics data with different parametric models (Table 1), we find that two models, CREX1 and HYB, are unable to correctly reproduce the data and can be rejected while five models, STEP3P, CREX2, CREX3, CRELH, and HYBM, provide acceptable fits (rms $\leq 2.56 \times 10^{-3}$). However, if we take into account the number of adjustable parameters (I_B), HYBM is better than STEP3P but not as good as CREX2 or even CRELH, and CREX3 does not enhance significantly the fit quality compared to CREX2 and is not retained. So, the best fit of our data is obtained with CREX2.

Both STEP3P and HYBM involve three distinct species with exponential time contributions and give evidence of two timescales for the solvation processes, a short one of a few picoseconds and a long one of a couple of tens of picoseconds. Indeed, the lifetime of the first species, e^-_{wb}, in STEP3P (1.3 ps,

TABLE 3: Parameters of CREX2 Model Resulting from the Probabilistic Analysis of the Experimental Data for the Solvation of the Electron in Ethylene Glycol

x	x_∞	Δ_{x1}	τ_{x1} (ps)	Δ_{x2}	τ_{x2} (ps)	$\langle t_x \rangle$ (ps)
ϵ	9000 M^{-1} cm^{-1}	-1695 ± 30 M^{-1} cm^{-1}	1.02 ± 0.02			1.0
E_{max}	2.219 eV	-0.26 ± 0.01 eV	1.71 ± 0.06	-0.12 ± 0.01 eV	25.5 ± 0.3	22.5
Ω	1.208 eV	0.42 ± 0.03 eV	$\tau_{E_{max}1}$	0.39 ± 0.03 eV	$\tau_{E_{max}2}$	23.9
γ	1.461	0.32 ± 0.12	$\tau_{E_{max}1}$	0.38 ± 0.12	$\tau_{E_{max}2}$	24.2

TABLE 4: Parameters of CRELH Model Resulting from the Probabilistic Analysis of the Experimental Data for the Solvation of the Electron in Ethylene Glycol

x	x_∞	Δ_x	τ_x (ps)	β_x	$\langle \tau_x \rangle$ (ps)	$\langle t_x \rangle$ (ps)
ϵ	9000 M^{-1} cm^{-1}	-1640 ± 35 M^{-1} cm^{-1}	1.03 ± 0.03	1	1.0	1.0
E_{max}	2.219 eV	-0.67 ± 0.04 eV	1.1 ± 0.2	0.35 ± 0.01	5.5	46.4
Ω	1.208 eV	0.86 ± 0.06 eV	6.6 ± 0.9	0.48 ± 0.03	14.3	47.2
γ	1.461	0.89 ± 0.06	6.2 ± 0.5	1	6.2	6.2

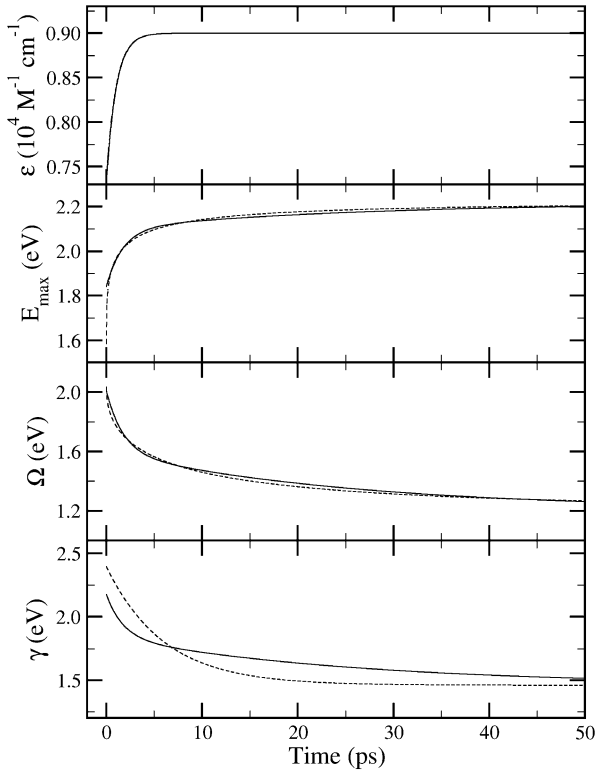

Figure 7. Time evolution of the spectral parameters, ϵ, the molar extinction coefficient, E_{max}, the peak position, Ω, the full width at half-maximum, and γ the asymmetry factor obtained by fitting the transient spectra with a biexponential ((—) CREX2) or a heterogeneous continuous relaxation model ((- - -) CRELH).

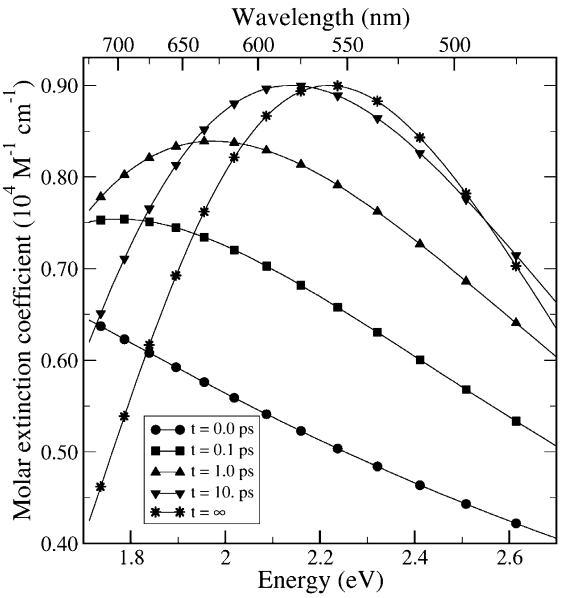

Figure 8. Time evolution of the electron absorption spectrum in the framework of the continuous relaxation model (CRELH) used to fit the experimental data.

TABLE 5: Parameters of HYBM Model Resulting from the Probabilistic Analysis of the Experimental Data for the Solvation of the Electron in Ethylene Glycol

x	x_1	x_∞	Δ_x	τ_x (ps)
ϵ	7175 ± 60	9000	3310 ± 115	2.1 ± 0.03
E_{max}	1.77 ± 0.01	2.219	-0.100 ± 0.001	22.3 ± 0.4
Ω	1.67 ± 0.03	1.208	0.34 ± 0.002	25.5 ± 0.1
γ	10	1.461	0.83 ± 0.04	$\tau_{E_{max}}$

Table 2) is of the same order of magnitude as τ_{12} and τ_ϵ, the characteristic times of the stepwise transition and the ϵ evolution of $e^-_{sb,2}$ in HYBM (2.4 and 2.1 ps, respectively, Table 5). Moreover, the lifetime of the intermediate species, e^-_{sb}, in STEP3P (Table 2) as well as the characteristic times, τ_{Emax}, τ_γ, and τ_Ω, for the homogeneous continuous spectral relaxation of $e^-_{sb,2}$ in HYBM (Table 5) is found to be close to 25 ps. This latter value resulting of a global data analysis is in agreement with the times determined by Kloepfer et al. in EG from transient signals at 500 nm obtained either by solvent photoinionization (27 ps) or by I^- photodetachment (25 ps).[17] The authors found somewhat different values from signals at 800 nm (8 and 17 ps, respectively).[17] Silva et al. studied the pump−probe spectroscopy of the equilibrated solvated electron in EG with three-pulse experiments.[61] The transient signals obtained at three different probe wavelengths were fitted separately by multiexponential functions providing various characteristic times but in the same time ranges. For all the signals, there is a fast component (~0.5 ps) followed by either one long component (42.3 ps at 660 nm) or two contributions (1.9 and 18.5 ps at 800 nm and 3.9 and 34 ps at 920 nm).[61] Previously, for the formation time of the solvated electron in EG, Chase and Hunt had given a crude estimation of 5 ps based only on signals observed at 1000 nm.[62] Miyasaka et al. also found a solvation time lower than 10 ps by analyzing only the transient signal recorded at peak absorbance after 266 nm two-photon photolysis using pulses with about 20 ps fwhm.[63] In our work, we prefer to perform a global analysis treating all the kinetic traces simultaneously in order to really extract the main characteristic times of solvation.

In the case of stepwise mechanisms applied to the solvation dynamics of electrons, several studies have suggested that the transition times are related to the dielectric relaxation times. For instance, Chase and Hunt established for several alcohols that the time of formation of e^-_s measured in the visible region,

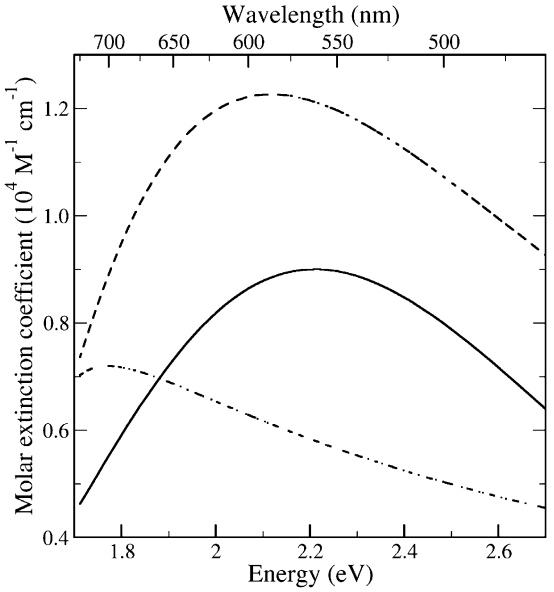

Figure 9. Absorption spectra of the species involved in the modified hybrid mechanism (HYBM) used to fit the experimental data: (···) $e^-_{wb,1}$, (- - -) $e^-_{sb,2}$ before any continuous shift, and (—) $e^-_{sb,2} \equiv e^-_s$ when the continuous shift is completed.

similar to the decay time determined at 1300 nm, was correlated with the dielectric relaxation time, τ_{D2}, which corresponds to the reorientation time of the monomer alcohol.[62] Hirata et al. indicated a correlation between the decay time measured in the near-IR region and the longitudinal relaxation time $\tau_{L1} = \tau_{D1}\epsilon_{\infty 1}/\epsilon_{01}$; τ_{D1} stands for the reorientation time that accompanies the intermolecular hydrogen bond breaking, and τ_{L1} accounts for the presence of an excess charge.[39] For EG, from analysis of permittivity measurements based on Debye relaxation processes, Barthel and Butchner reported values of 145 and 10 ps for τ_{D1} and τ_{D2}, respectively, with $\epsilon = \epsilon_{01} = 40.8$, $\epsilon_{\infty 1} = \epsilon_{02} = 7.3$, and $\epsilon_{\infty 2} = \epsilon_{03} = 3.8$ leading to 26 and 5.2 ps for τ_{L1} and τ_{L2}, respectively.[64] Consequently, we note a good correlation between our estimation of the long solvation time and the value of τ_{L1}. Nevertheless, this value is longer than the solvent relaxation time determined by means of femtosecond polarization spectroscopy using optical-heterodyne-detected Raman-induced Kerr-effect spectroscopy (OHD-RIKES).[65,66] Chang and Castner fitted the signal component arising from rotational diffusion of the solvent molecules to a multiexponential decay law.[65] They found two characteristic times $\tau_{1,rot} = 0.65$ ps and $\tau_{2,rot} = 9.37$ ps and determined from the dipolar solvation dynamics correlation function an effective solvation time of $\tau_s = 1.76$ ps for EG. More recently, Giraud and Wynne analyzed their OHD-RIKES data for EG with a multimode Brownian-oscillator model and determined for the low-frequency part of the spectrum corresponding with rotational diffusion in the liquid the time of rise and decay to be ~0.25 and ~16 ps, respectively.[66]

The best adjustments of our data are obtained with the continuous relaxation models, CRELH and CREX2. Those models involve only one relaxing species but account for spatial heterogeneity as all the spectral parameters (ϵ, E_{max}, Ω, γ) are time-dependent and evolve according to specific stretched exponential (Table 4) or biexponential functions (Table 3). A degree of inhomogeneity in the liquid EG has already been invoked by Giraud and Wynne.[66] With the CREX2 model, we have found two characteristic times ($\tau_1 = 1.0$ or 1.7 ps and $\tau_2 = 25.5$ ps) very similar to those already obtained by STEP3P or HYBM models corroborating the presence of these two time

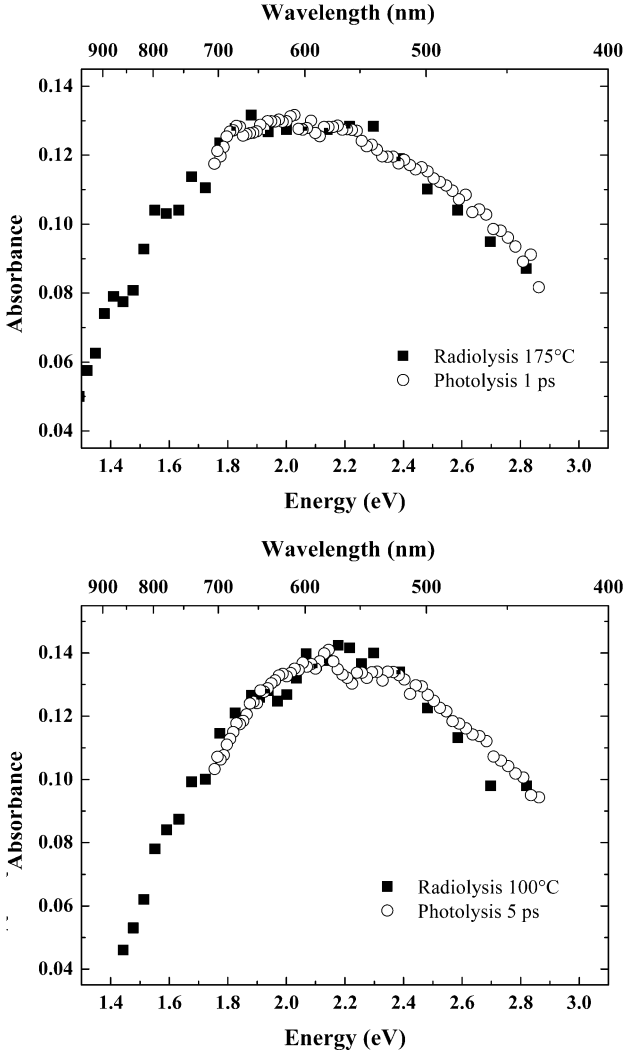

Figure 10. Comparison between the absorption spectra recorded in ethylene glycol at early time after photoionization at 263 nm (○) and the absorption spectra of the solvated electron obtained in ethylene glycol at high temperature by pulse radiolysis (■) (taken from ref 65).

scales in the electron solvation in EG. With the CRELH model, the values of the defined average relaxation times and lifetimes are not really physically significant. However, the values of $\beta_x < 0.5$ obtained for E_{max} and Ω suggest very nonexponential solvent response, that is, very broad distribution of exponential relaxation times or coexistence of different coupled time scales. So, the relaxation time has to be seen as a spatially varying quantity. Our results differ markedly from that obtained by Sudo et al. from dielectric measurements.[67] They performed a fitting procedure for the frequency dependence of the complex permittivity using the stretched exponential function (Kolhrausch−Williams−Watts function) and determined the parameter β_K for the asymmetrical broadness of the relaxation curve and the relaxation time τ to be 0.935 and ~120 ps, respectively. Consequently, as $\beta_K < 1$, the dielectric loss for EG shows an asymmetric broadening (interpreted with a heterogeneous structure such as the variation of the size and dynamical structure of a cooperative domain), but as β_K is close to 1 the heterogeneity is weak. Moreover, the value of τ is close to that of τ_{D1} found by Barthel and Butchner considering Debye-type (exponential) relaxation.[64] The fact that the dielectric relaxation occurs on a time scale (1 order of magnitude higher than that of the solvation process) on which the solvent appears roughly homogeneous, in contrast to the great heterogeneous solvation

of the electron, suggests that dielectric relaxation and solvation process do not probe the same solvent response. Solvation dynamics reveals the collective orientational response of the solvent in the immediate vicinity of the electron (monomeric rotation and rotational orientation of OH group) and not the global response corresponding to rotation of polymeric clusters due to a hydrogen bond.

So, the question arises whether the bound electron is an identifiable intermediate or a continuously changing state. The absence of isobestic point and the gradual blue shift of the absorption band of electron observed in the tens of picosecond range in the explored spectral window strongly suggest that the solvation process is a continuous process. In stepwise models, addition of a third intermediate state (STEP4) enhances slightly the fit quality compared to STEP3; the spectrum of this third species lies between that of e_{sb}^- and that of e_s^- (Figure 5) indicating a regular evolution from state to state which conforms to the hypothesis of a continuous relaxation process. Nevertheless, that relaxation cannot be described by exponential evolution. Further evidence for a continuous solvation may be the time−temperature analogy. Indeed, we notice that the transient spectra recorded at 1 and 5 ps after the photoionization at room temperature are similar to the spectra of the solvated electron in the equilibrated state at higher temperatures, 175 and 100 °C, respectively[68] (Figure 9). Those spectral resemblances indicate similar solvent organization disorder (which increases with T or as t tends to 0). That analogy between time and temperature has already been made by Madsen et al. for water.[50] They reported in the case of two-photon ionization of water at 4.65 eV that the spectral blue shift observed in the absorption spectrum of the hydrated electron after 1 ps was purely continuous and accurately described by the well-known analytical expression for the temperature-dependent absorption spectrum of the ground-state hydrated electron. Lately, Crowell and co-workers invoked a possible temperature jump in multiphoton ionization of liquid water by 400 nm terawatt light to cause power-dependent ultrafast kinetics of electrons.[69]

The fact that the solvation process seems to be a continuous process in our experimental conditions suggests that the photogenerated electrons are rapidly trapped, with a characteristic time shorter than our temporal resolution and that the observed electrons are only localized electrons. It has already been reported that, for all the alcohols, the electron trapping is less than 1 ps.[15] The presence of numerous preexisting traps in the molecular liquid structure may account for such a fast trapping process. Kenney-Wallace and Jonah found that electrons rapidly solvate in EG at times of <5 ps and presumed that chelate-like local structures in the liquid offer abundant preexisting trapping sites.[13] For liquid EG, traps could correspond to reported dimer conformations and/or to the most probable local structure of molecules formed by three nearest neighbors, of which half are on average accepting and half are donating protons to the three intermolecular hydrogen bonds.[59]

5. Conclusion

The formation of the equilibrated solvated electron in ethylene glycol was followed using pump−probe transient absorption spectroscopy in the visible spectral range from 425 to 725 nm. The electron was generated with a 263 nm femtosecond laser pulse by the photoionization of the solvent according to a two-photon absorption process. The two-photon absorption coefficient of ethylene glycol at 263 nm was estimated to be $\beta = (2.1 \pm 0.2) \times 10^{-11}$ m W^{-1}. The excess electron in EG presents a wide absorption band in the visible and the near-IR at very short delay time after the pump pulse. The time-resolved spectra revealed that a localized electron which absorbs in the blue spectral domain is quickly formed and relaxes to the equilibrated solvated electron in the picosecond time range.

Using Bayesian data analysis method, we performed a fitting procedure of the spectrokinetics signals with different solvation models. That analysis clearly indicates that it is not obvious to select a unique model to describe the solvation dynamics of the electron in EG. We showed that four models are able to reproduce correctly the data: a two-step model, a heterogeneous or biexponential continuous relaxation model, a hybrid model associating a stepwise transition and homogeneous continuous relaxation. From the stepwise, the biexponential relaxation, and the hybrid models, we deduce that two time constants characterize the dynamic behavior of the solvated electron in EG: a fast time of about 1−2 ps and a second longer one of around 25 ps. Nevertheless, the best fit is given by the continuous spectral relaxation model. The fact that the time-evolution of the absorption spectrum of the solvated electron in EG can be accurately described by the temperature-dependent absorption spectrum of the ground-state solvated electron suggests that the spectral blue shift is mostly caused by the continuous relaxation of the electron trapped in a large distribution of solvent cages.

6. Appendix

In this study, absorption spectra have been modeled by three-parameter log-normal functions (peak position E_{max}, full width at half-maximum Ω, and asymmetry factor γ):

$$S(E; E_{max}, \Omega, \gamma) = u^{-1} \exp\left(-\frac{1}{2}(\sigma^2 + \ln^2(u)/\sigma^2)\right) \quad (30)$$

where the auxiliary parameters are defined by

$$\sigma = \ln(\gamma)/2\sqrt{2} \quad (31)$$

$$u = (E - \vartheta)/m \quad (32)$$

$$m = \Omega/[2 \exp(-\sigma^2) \sinh(\ln \gamma)] \quad (33)$$

$$\vartheta = E_{max} - m \exp(-\sigma^2) \quad (34)$$

The normalization is chosen such that the maximal value is $S(E_{max}; E_{max}, \Omega, \gamma) = 1$; accordingly, the peak area is

$$I_S = \sqrt{2\pi} m\sigma \exp(-\sigma^2/2) \quad (35)$$

References and Notes

(1) Hart, E. J.; Boag, J. W. *J. Am. Chem. Soc.* **1962**, *84*, 4090.
(2) Boag, J. W.; Hart, E. J. *Nature* **1963**, *197*, 45.
(3) Keene, J. P. *Nature* **1963**, *197*, 47.
(4) Hart, E. J.; Anbar, M. *The Hydrated Electron;* Wiley-Interscience: New York, 1970.
(5) Jou, F. Y.; Dorfman, L. M. *J. Chem. Phys.* **1973**, *58*, 4715.
(6) Nikogosyan, D. N.; Oraevsky, A. A.; Rupasov, V. I. *Chem. Phys.* **1983**, *77*, 131.
(7) Migus, A.; Gauduel, Y.; Martin, J. L.; Antonetti, A. *Phys. Rev. Lett.* **1987**, *58*, 1559.
(8) Gauduel, Y.; Pommeret, S.; Migus, A.; Antonetti, A. *J. Phys. Chem.* **1989**, *93*, 3880.
(9) Reuther, A.; Laubereau, A.; Nikogosyan, D. N. *J. Phys. Chem.* **1996**, *100*, 16794.
(10) Crowell, R. A.; Bartels, D. M. *J. Phys. Chem.* **1996**, *100*, 17940.
(11) Thomsen, C. L.; Madsen, D.; Keiding, S. R.; Thogersen, J.; Christiansen, O. *J. Chem. Phys.* **1999**, *110*, 3453.
(12) Hertwig, A.; Hippler, H.; Unterreiner, A.-N. *Phys. Chem. Chem. Phys.* **1999**, *1*, 5633.
(13) Kenney-Wallace, G. A.; Jonah, C. D. *J. Phys. Chem.* **1982**, *86*, 2572.

(14) Shi, X.; Long, F. H.; Lu, H.; Eisenthal, K. B. *J. Phys. Chem.* **1995**, *99*, 6917.
(15) Goulet, T.; Pépin, C.; Houde, D.; Jay-Gerin, J.-P. *Radiat. Phys. Chem.* **1999**, *54*, 441.
(16) Scheidt, T.; Laenen, R. *Chem. Phys. Lett.* **2003**, *371*, 445.
(17) Kloepfer, J. A.; Vilchiz, V. H.; Lenchenkov, V. A.; Germaine, A. C.; Bradforth, S. E. *J. Chem. Phys.* **2000**, *113*, 6288.
(18) Soroushian, B.; Lampre, I.; Pernot, P.; De Waele, V.; Pommeret, S.; Mostafavi, M. *Chem. Phys. Lett.* **2004**, *394*, 313.
(19) Brun, R.; Reichert, P.; Kunsch, H. R. *Water Resour. Res.* **2001**, *37*, 1015.
(20) D'Avignon, D. A.; Bretthorst, G. L.; Holtzer, M. E.; Holtzer, A. *Biophys. J.* **1988**, *74*, 3190.
(21) D'Avignon, D. A.; Bretthorst, G. L.; Holtzer, M. E.; Holtzer, A. *Biophys. J.* **1999**, *76*, 2752.
(22) Holtzer, M. E.; Bretthorst, G. L.; D'Avignon, D. A.; Angeletti, R. H.; Mints, L.; Holtzer, A. *Biophys. J.* **2001**, *80*, 939.
(23) Renou, F.; Mostafavi, M.; Archirel, P.; Bonazzola, L.; Pernot, P. *J. Phys. Chem. A* **2003**, *107*, 1506.
(24) Renou, F.; Pernot, P.; Bonin, J.; Lampre, I.; Mostafavi, M. *J. Phys. Chem. A* **2003**, *107*, 6587.
(25) Renou, F.; Archirel, P.; Pernot, P.; Levy, B.; Mostafavi, M. *J. Phys. Chem. A* **2004**, *108*, 987.
(26) Vilchiz, V. H.; Kloepfer, J. A.; Germaine, A. C.; Lenchenkov, V. A.; Bradforth, S. E. *J. Phys. Chem. A* **2001**, *105*, 1711.
(27) Pépin, C.; Goulet, T.; Houde, D.; Jay-Gerin, J.-P. *J. Phys. Chem. A* **1997**, *101*, 4351.
(28) Sivia, D. S. *Data Analysis: A Bayesian Tutorial*; Clarendon: Oxford, U.K., 1996.
(29) D'Agostini, G. *Bayesian Reasoning in Data Analysis*; World Scientific Publishing: River Edge, NJ, 2003.
(30) Dose, V. *Rep. Prog. Phys.* **2003**, *66*, 1421.
(31) Gilks, W. R.; Richardson, S.; Spiegelhalter, D. J. *Markov Chain Monte Carlo in Practice*; Chapman and Hall: London, 1996.
(32) Wasserman, L. *J. Math. Psychol.* **2000**, *44*, 92.
(33) Jung, J.-M. *Research Habilitation Report;* Louis Pasteur University, Strasbourg I: Strasbourg, France, 2003.
(34) Pommeret, S.; Gobert, F.; Mostafavi, M.; Lampre, I.; Mialocq, J.-C. *J. Phys. Chem. A* **2001**, *105*, 11400.
(35) Shen, Y. R. *The Principles of Nonlinear Optics*; John Wiley and Sons: New York, 1984.
(36) Sutherland, R. L. *Handbook of Nonlinear Optics*; Marcel Dekker: New York, 1996.
(37) The fitted value of R is quite large compared to the calculated value with the refractive indexes (0.037). This discrepancy is due to the surface roughness of the jet that induces additional scattering.
(38) Dragomir, A.; McInerney, J. G.; Nikogosyan, D. N.; Ruth, A. A. *IEEE J. Quantum Electron.* **2002**, *38*, 31.
(39) Hirata, Y.; Mataga, N. *J. Phys. Chem.* **1990**, *94*, 8503.
(40) Pépin, C.; Goulet, T.; Houde, D.; Jay-Gerin, J.-P. *J. Phys. Chem.* **1994**, *98*, 7009.
(41) Assel, M.; Laenen, R.; Laubereau, A. *J. Chem. Phys.* **1999**, *111*, 6869.
(42) Holpar, P.; Megyes, T.; Keszei, E. *Radiat. Phys. Chem.* **1999**, *55*, 573.
(43) Lorenc, M.; Ziolek, M.; Naskrecki, R.; Karolczak, J.; Kubicki, J.; Maciejewski, A. *Appl. Phys. B* **2002**, *74*, 19.
(44) Ekvall, K.; van der Meulen, P.; Dhollande, C.; Berg, L.-E.; Pommeret, S.; Naskrecki, R.; Mialocq, J.-C. *J. Appl. Phys.* **2000**, *87*, 2340.
(45) Shkrob, I. A.; Oulianov, D. A.; Crowell, R. A.; Pommeret, S. *J. Appl. Phys.* **2004**, *96*.
(46) Long, F. H.; Lu, H.; Eisenthal, K. B. *Phys. Rev. Lett.* **1990**, *64*, 1469.
(47) Gustavsson, T.; Baldacchino, G.; Mialocq, J.-C.; Pommeret, S. *Chem. Phys. Lett.* **1995**, *236*, 587.
(48) Jou, F. Y.; Freeman, G. R. *Can. J. Chem.* **1976**, *54*, 3693.
(49) Jou, F. Y.; Freeman, G. R. *J. Phys. Chem.* **1979**, *83*, 2383.
(50) Madsen, D.; Thomsen, C. L.; Thogersen, J.; Keiding, S. R. *J. Chem. Phys.* **2000**, *113*, 1126.
(51) Okazaki, K.; Freeman, G. R. *Can. J. Chem.* **1978**, *56*, 2305.
(52) Richert, R. *J. Phys.: Condens. Matter* **2002**, *14*, R703.
(53) Sauer, M. C.; Arai, J., S.; Dorfman, L. M. *J. Chem. Phys.* **1965**, *42*, 708.
(54) Jou, F. Y.; Freeman, G. R. *J. Phys. Chem.* **1979**, *83*, 261.
(55) Pommeret, S.; Antonetti, A.; Gauduel, Y. *J. Am. Chem. Soc.* **1991**, *113*, 9105.
(56) Pachler, K. G. R.; Wessels, P. L. *J. Mol. Struct.* **1970**, *6*, 471.
(57) Schwartz, M. *Spectrochim. Acta* **1977**, *33A*, 1025.
(58) Saiz, L.; Padro, J. A.; Guardia, E. *J. Chem. Phys.* **2001**, *114*, 3187.
(59) Bako, I.; Grosz, T.; Palinkas, G.; Bellissent-Funel, M.-C. *J. Chem. Phys.* **2003**, *118*, 3215.
(60) Petterson, K. A.; Stein, R. S.; Drake, M. D.; Roberts, J. D. *Magn. Reson. Chem.* **2005**, *43*, 225.
(61) Silva, C.; Walhout, P. K.; Reid, P. J.; Barbara, P. F. *J. Phys. Chem. A* **1998**, *102*, 5701.
(62) Chase, W. J.; Hunt, J. W. *J. Phys. Chem.* **1975**, *79*, 2835.
(63) Miyasaka, H.; Masuhara, H.; Mataga, N. *Laser Chem.* **1987**, *7*, 119.
(64) Barthel, J.; Buchner, R. *Pure Appl. Chem.* **1991**, *63*, 1473.
(65) Chang, Y. J.; Castner, E. W. *J. Chem. Phys.* **1993**, *99*, 7289.
(66) Giraud, G.; Wynne, K. *J. Chem. Phys.* **2003**, *119*, 11753.
(67) Sudo, S.; Shinyashiki, N.; Kitsuki, Y.; Yagihara, S. *J. Phys. Chem. A* **2002**, *106*, 458.
(68) Mostafavi, M.; Lin, M.; He, H.; Muroya, Y.; Katsumura, Y. *Chem. Phys. Lett.* **2004**, *384*, 52.
(69) Crowell, R. A.; Lian, R.; Shkrob, I. A.; Qian, J.; Oulianov, D. A.; Pommeret, S. *J. Phys. Chem. A* **2004**, *108*, 9105.